

New method to describe the zonal symmetries and asymmetries of the Southern Annular Mode

Elio Campitelli * and Leandro Díaz

*Universidad de Buenos Aires, Facultad de Ciencias Exactas y Naturales, Departamento de
Ciencias de la Atmósfera y los Océanos, Buenos Aires, Argentina CONICET – Universidad de
Buenos Aires, Centro de Investigaciones del Mar y la Atmósfera (CIMA), Buenos Aires, Argentina
CNRS – IRD – CONICET – UBA, Instituto FrancoArgentino para el Estudio del Clima y sus
Impactos (UMI 3351 IFAECI), Buenos Aires, Argentina*

Carolina Vera

¹⁰ *Corresponding author: Elio Campitelli, elio.campitelli@cima.fcen.uba.ar

ABSTRACT

11 Enter the text of your abstract here. This is a sample American Meteorological Society (AMS)
12 \LaTeX template. This document provides authors with instructions on the use of the AMS \LaTeX tem-
13 plate. Authors should refer to the file `amspaper.tex` to review the actual \LaTeX code used to create
14 this document. The `template.tex` file should be modified by authors for their own manuscript.

15 *Significance statement.* This is significant because I wrote it.

16 **1. Introduction**

17 The Southern Annular Mode (SAM) is the main mode of variability in the Southern Hemisphere
18 extratropical circulation (Rogers and van Loon 1982) in daily, monthly, and decadal timescales
19 [Baldwin (2001); Fogt2006] and exerts an important influence in weather conditions such as
20 temperature and precipitation anomalies and sea ice concentration (Fogt and Marshall 2020). Its
21 positive phase is traditionally described as anomalously low pressures over Antarctica surrounded
22 by a ring of anomalous high pressures in middle-to-high latitudes.

23 However, computed as the leading Empirical Orthogonal Function (EOF) of Sea Level Pressure
24 or low-level geopotential height, the SAM spatial structure contains noticeable deviations from this
25 zonally symmetric description, particularly in the Pacific Ocean region. These zonal asymmetries
26 are not widely studied, but previous work suggest that they strongly modulate the regional impacts of
27 the SAM, going as far as reversing its relationship between precipitation in South America (Silvestri
28 and Vera 2009). At the very least, the fact that the SAM is not entirely zonally symmetric hinders
29 our ability to reconstruct its historical variability prior to the availability of dense observations in
30 the Southern Hemisphere (Jones et al. 2009).

31 We are not aware of any previous work which quantifies the temporal variability of the asymmetric
32 component of the SAM with the exception of Fogt et al. (2012). However, their methods based
33 on composites of positive and negative SAM events leads to some issues, such as spatial patterns
34 derived from as little as 4 cases and from imbalanced periods (for example, 5 of the 7 cases in
35 their DJF SAM+ composite are from later than 1988, whereas all of the 8 years in their DJF SAM-
36 composite are from earlier than 1988). This is particularly important due to the inhomogeneities

37 in reanalysis products prior to the satellite era and the possible change in the asymmetric structure
38 of the SAM (Silvestri and Vera 2009).

39 Our objective is, then, to systematically characterise the zonally asymmetric component of the
40 SAM variability by constructing two indices which aim to capture exclusively the variability of
41 the symmetric and asymmetric component each. We then analyse their temporal variability, trends
42 and vertical coherence. We study the spatial patterns described by the variability exclusive to each
43 index. Finally, we investigate their relationship with temperature and precipitation anomalies.

44 **2. Methods**

45 **1) DATA**

46 To describe the Southern Annular Mode and its variability we used monthly geopotential height
47 at 2.5° longitude by 2.5° latitude of horizontal resolution and 37 vertical isobaric levels from ERA5
48 (Hersbach et al. 2020) for the period 1979 to 2018. We restrict our analysis to the post-satellite era
49 to avoid any confounding factors arising from the introduction of satellite observations.

50 We describe the relationship between the SAM indices and temperature and precipitation. We
51 use temperature data from NOAA's Merged Land Ocean Global Surface Temperature Analysis
52 V4.0.1 (Vose et al. 2012; Smith et al. 2008), which blends land and ocean temperature analysis into
53 a monthly global grid 5° latitude by 5° longitude. For precipitation, we use monthly, 0.5° latitude
54 by 0.5° longitude data from the Global Precipitation Climatology Centre (Schneider et al. 2015).

55 **2) DEFINITION OF INDICES**

56 Traditionally the Southern Annular Mode (SAM) is defined as the leading Empirical Orthogonal
57 Mode (EOF) of sea level pressure or geopotential height at lower levels (Ho et al. 2012). Following
58 Baldwin and Dunkerton (2001), we extend that definition vertically and use the term SAM to refer

59 to the the leading EOF of the monthly anomalies of geopotential field south of 20°S at each level.
60 We performed EOFs by computing the Singular Value Decomposition of the data matrix consisting
61 in 481 rows and 4176 columns (144 points of longitude and 29 points of latitude). We weighted
62 the values by the square root of the cosine of latitude to account for the non-equal area of each
63 gridpoint (Chung and Nigam 1999).

64 To separate between the zonally symmetric and asymmetric components of the SAM, we com-
65 puted the zonal mean and anomalies of the full SAM spatial pattern, as shown in Figure 1 for
66 700hPa. The full spatial signal ($\text{EOF}_1(\lambda, \phi)$) is the sum of the zonally asymmetric ($\text{EOF}_1^*(\lambda, \phi)$)
67 and symmetric ($[\text{EOF}_1](\lambda, \phi)$) components. We then compute the “Full SAM”, “Asymmetric
68 SAM” and “Symmetric SAM” indices as the regression coefficients of the regression of each
69 monthly geopotential field on the respective patterns (weighting by the cosine of latitude). The
70 three indices are normalised by dividing them by the standard deviation of the “Full” index at each
71 level. As a result, the magnitude between indices is comparable. However, only “Full” index will
72 have unit standard deviation per definition. From the regression, we also use the explained variance
73 of each pattern as a indication of the degree of symmetry or asymmetry of each monthly field.

74 Our method assumes linearity in the asymmetric component of the SAM. That is, we assume that
75 zonal symmetries associated with positive SAM are opposite and equal to the ones associated with
76 negative SAM. Fogt et al. (2012)’s composites (their Figure 4) suggest that this might not be entirely
77 valid, although we argue that much of that apparent non-linearity is due to the heterogeneous nature
78 of the selected years for constructing the composites. Using our data (from 1979 to 2018), seasonal
79 composites of zonal anomalies of 700 hPa geopotential height for SAM+ (Full SAM index greater
80 than 1 standard deviation) and SAM- (smaller than negative 1 standard deviation) show relatively
81 high pattern correlations all seasons and are visually very linear (Figure A9). Therefore, we believe
82 that our method is at the very least a reasonable approximation of the phenomenon.

By computing a single EOF pattern using data for all months we are assuming that the zonal anomalies of the SAM are the same in all seasons. Geopotential zonal anomalies computed by projecting the first EOF *of each season* are very similar to each other (Figure A10) and show pattern correlations between 0.65 (DJF with JJA) and 0.9 (between MAM and SON). Based on this, we believe that our initial assumption is not unreasonable.

Finally, we assume that the zonally asymmetric pattern is stationary in time. Silvestri and Vera (2009) suggest that this might not be the case between 1958 and 2004 but the period we analyse is much shorter (1979-2018) so it's unlikely that we could observe significant changes. Moreover, zonal asymmetry of the spatial patterns for the two halves of the period (1979 to 1998 and 1999 to 2018) show no systematic change (Figure A11).

3) REGRESSIONS

We perform linear regression to quantify the association between the SAM indices and other variables. Since the Asymmetric and Symmetric SAM indices are significantly correlated with each other, to capture the variability explained uniquely by each index we use one multiple linear regression instead of two simple linear regressions. To obtain the linear coefficients of a variable X (geopotential, temperature, precipitation, etc...) with the Asymmetric SAM (SAM_a) and Symmetric SAM (SAM_s) we fit the equation

$$X(\lambda, \phi, t) = \alpha(\lambda, \phi)SAM_a + \beta(\lambda, \phi)SAM_s + X_0(\lambda, \phi) + \epsilon(\lambda, \phi, t)$$

where λ and ϕ are the longitude and latitude, t is the time, α and β are the linear coefficients, X_0 and ϵ are the constant and error terms. From this equation, α represents the (linear) association of X with the variability of the Asymmetric SAM that is not explained by the variability of

the Symmetric SAM; in other words, it is proportional to the partial correlation of X and the Asymmetric SAM, controlling for the effect of the Symmetric SAM and viceversa for β .

At 2.5° by 2.5° resolution, a single regression field is composed of thousands of regressions. In such case, using naive p-values to test for significance leads to misleading results (Walker 1914; Katz and Brown 1991). While there are multiple proposed solutions in the literature, Wilks (2016) suggests that adjuncting p-values by controlling for the False Discovery Rate (Benjamini and Hochberg 1995) is a simple and effective method to ameliorate this issue. Therefore, p-values showed in regression fields are all adjusted following Benjamini and Hochberg (1995).

When performing a separate regression for each trimester (DJF, MAM, JJA, SON) we first average the relevant variables to obtain a single value for each year and each trimester.

3. Results

a. Temporal evolution

The temporal evolution of the Assymmetric and Symmetric SAM was firstly assessed. Figure 2 shows the corresponding time series for 700 hPa and 50 hPa and their corresponding density estimates. We selected these two levels as representative of the tropospheric and stratospheric variability respectively. As will be shown later, both indices are highly coherent within each atmospheric layer, therefore is reasonable to take one level as representative of each layer.

Month-to-month variability is evident for both indices, with noisy variations in the low frequency. At first glance the series can be distinguished by their distributions. Compared to the stratospheric indices, the stratospheric indices are much more long-tailed; that is, extreme values (both negative and positive) abound. The Asymmetric series have both more variability in the higher frequencies than the Symmetric series.

125 The stratospheric Symmetric SAM varies strongly with a two-year period, which can be seen by
126 spectral analysis (Figure A3). This might suggests a link between stratospheric SAM variability
127 and QBO. There is a local peak at 2 years in the periodigram of the tropospheric Symmetric SAM
128 also, although it's not statistically significant. In the troposphere the most significant peak of
129 variability is found in the Asymmetric index at around 3.6 months.

130 From Figure 2 we can see that the Asymmetric and Symmetric time series appear to be correlated.
131 Moreover, looking at the extremes in the stratosphere, the Symmetric serie appears to lag the
132 Asymmetric series (see, for example, the positive events on late 1987). We show these correlations,
133 across all the levels of the reanalysis for zero and -1 lag (Asymmetric index leading the Symmetric
134 index), in Figure 3. Zero-lag correlations between the Asymmetric and Symmetric series are
135 relatively constant throught the troposphere, fluctiating between 0.39 and 0.45. One-month-lag
136 correlations are similarly constant but significantly reduced to around 0.17. In the stratosphere,
137 zero-lag correlations drop to a minimum of 0.21 at 20 hPa and then it increases again monotonically
138 with height up to the uppermost level of the reanalysis (although results near the top of the models
139 are to be interpreted with care). At the same time, one-month-lag correlations increase with height.
140 As a consequence, statospheric Symmetric index tend to precede corresponding Asymmetric index.

141 Figure 4a shows (zero-lag) cross-correlation across levels for the Full, Symmetric and Asym-
142 metric SAM indices. For the Full SAM (panel a), high values below 100 hPa reflect the vertical
143 (zero-lag) coherency throughout the troposphere. Above 100 hPa correlation between levels falls off
144 more rapidly, indicating less coherent (zero-lag) variability. Therefore, there is a non negligible
145 correlation between the troposphere and the lower-to-middle stratosphere. Examining panels b and
146 c, we see that the Asymmetric and Symmetric SAM share the same high level of coherency in the
147 troposphere but they differ in their stratospheric behaviour. Stratospheric coherency is stronger

for the Asymmetric SAM than the Symmetric SAM. The stratospheric Symmetric SAM seems to connect more strongly to the troposphere than the Asymmetric SAM.

The trends for each of the indices (Full, Symmetric, Asymmetric) were evaluated for the whole period 1979-2018 at each level (Figure 5) for the whole year and separated by trimesters. The Full SAM index presents a statistically significant trend (panel a.1) that extends throughout the troposphere up to about 50 hPa and reaches its maximum value at 100 hPa. The seasonal trends (rest of column a) indicate that positive trends are present in Autumn and particularly in Summer, where the 100 hPa maximum is much more defined. Positive trends have been documented by previous studies (e.g. Fogt and Marshall 2020, and references therein) using indices of the SAM based on surface or near-surface circulation.

By separating the SAM signal in its Asymmetric and Symmetric parts, we can not only see that these trends are almost entirely due to the Symmetric component (column b vs. column c), but in some cases the trends become more clear. In Summer, the Asymmetric SAM has a statistically non significant negative trend in the middle troposphere that obscures the trend in the Full index; as a result, trends computed using only the Symmetric component are more clear (compare the shading region in panel a.2 and c.2). In Autumn, using the Symmetric SAM reveals a statistically significant positive trend in the stratosphere that is not significant using the Full index.

We stress that these are only linear trends during the whole period and the absence of a statistically significant signal should not be taken as evidence of no systematic change. In particular, going back to Figure 2, we can see an evident change in the stratospheric Asymmetric component (red line in panel a) between the 90's, when we see a dominance of extreme negative values, and the 00's, when we see the inverse. This change is restricted to the Winter months: the linear trend for JJA starting in 1990 for the Asymmetric component at 50hPa is 0.37 ± 0.22 .

Figure 6 shows decadal trends for the explained variance of each index. There is no evidence of a significant trend in the stratosphere. In the troposphere, there is a positive trend for the Asymmetric SAM and no significant trend for the Symmetric SAM. This suggests that the SAM has become more asymmetric in the period from 1979 to 2018. The change is slight, though; of the order of 1% increased explained variance per decade.

b. Spatial patterns

To show if, and to what extent, the Asymmetric and Symmetric SAM indices indeed capture the asymmetric and symmetric component of the SAM respectively, we computed the spatial regression of geopotential height anomalies on these indices and the Full SAM index. Figure 7 shows these regressions. Regression coefficients in column a are computed using the Full SAM. Regression coefficients in columns b and c are computed using multiple regression using the Asymmetric and Symmetric indices at the same time. Thus, they are to be interpreted as the patterns associated with each index, removing the variability (linearly) explained by the other index.

In the stratosphere, the spatial pattern associated with the Full SAM is more clearly dominated by a zonally symmetric, monopolar structure (panel a.1) which is, however, not perfectly centered in the South Pole. The monopole obtained by multiple regression with the Asymmetric and Symmetric SAM (panel c.1) is much more symmetric and the shift from total symmetry is captured by the regression pattern of the Asymmetric SAM as a wave-1 with maximum anomalies above the Belinghausen Sea on the Western Hemisphere and Davids Sea in the Eastern Hemisphere (panel b.1).

In the troposphere, panel a.2 shows the well known combination of zonally symmetrical annular mode with zonal asymmetries in the form of a wave-3. The regression using the Asymmetric and

194 Symmetric SAM indices successfully disentangle both structures. The Asymmetric component
195 gives rise to a cleaner zonal wave (panel b.2) and the Symmetric component is associated with an
196 trully annular mode, almost devoid of zonal asymmetries (panel c.2). The wave-3 pattern observed
197 in panel b.2 is rotated by half a wavelength from the average position of the mean wave-3 pattern
198 asociated with Raphael (2004)'s ZW3 index, whose reference locations are marked with points in
199 the figure. Thus, the tropospheric Asymmetric SAM index represents a zonal displacement in the
200 position of the climatological wave-3 pattern.

201 The amplitude of first zonal wave numbers at each latitude at 50 hPa and 700 hPa is shown in
202 Figure 8, where wave number zero represents the amplitude of the zonal mean. Column b shows
203 that the Asymmetric SAM is overwhelmingly dominated by wave 1 in the stratosphere (panel b),
204 while in the troposphere it is composed of zonal waves 3 to 1 in decreasing level of importance
205 (panel b). Looking at panel b.2 from Figure 7, it becomes apparent that zonal wavess 1 and 2
206 modulate the amplitude of zonal wave 3, which –as mentioned before– is larger in the Western
207 Hemisphere than in the Easten Hemisphere.

208 To analyse the vertical structure of the geopotential anomalies asociated with the asymmetric
209 SAM index, we show a vertical cross section of regressions of mean geopotential height between
210 65°S and 40°S for the 50 hPa Asymmetric SAM index (panel a) and for the 700 hPa Asymmetric
211 SAM index (panel b) (Figure 9). The geopotential anomalies associated with the stratospheric
212 Asymmetric SAM (panel a) are clearly constrained to the stratosphere, which underscores the
213 uncoupling between the stratospheric and tropospheric Asymmetric SAM. The vertical structure
214 of this signal tilts about 60° to the West between 100 hPa and 1 hPa, suggesting baroclinic processes.
215 Interestingly, the signal in the stratosphere maximises near 10 hPa despite using the 50 hPa index
216 for the regression.

217 The tropospheric Asymmetric SAM (panel b) has significant signals that extend upwards to the
218 uppermost levels of the reanalysis. In the troposphere, the wave-3 structure is equivalent barotropic
219 with maximum amplitude at roughly 250 hPa. The anomalies are much more intense in the Western
220 hemisphere, where they extent into the stratosphere. In the Eastern hemisphere the wave-3 signal
221 is weaker and confined to the troosphere while negative anomalies dominate in the stratosphere.
222 So, while the tropospheric Asymmetric SAM index is associated with stratospheric geopotential
223 anomalies, these do not project strongly onto the stratospheric Asymmetric SAM.

224 The structures shown in panels a and b in Figure 9 are surprisignly robust to the choice of index
225 level. For any stratospheric (above 100 hPa) index, the resulting anomalies are very similar to the
226 wave-1 structure with maximum near 10 hPa in panel a. Conversely, for any tropospheric (below
227 100 hPa) index, the result is very similar to panel b. The patterns mainly change in amplitude.

228 The wave-3 pattern from Figure 7 panel b.2 is very similar to the Pacific-South American Pattern
229 (Mo and Ghil 1987; Kidson 1988) which is a teleconnection pattern associated with the ENSO
230 (Karoly 1989). Indeed, Fogt et al. (2011) showed that there is a significant relationship between
231 the SAM and the ENSO. The correlation between the full SAM and the ENSO as measured by
232 the Oceanic Niño Index (Bamston et al. 1997) (ONI) is -0.16. Consistent with Fan (2007), we
233 show that this relationship is captured entirely the Asymmetric SAM, as this index has a partial
234 correlation of -0.26 with the ONI controlling for the effect of the Symmetric SAM, whereas the
235 Symmetric SAM's partial correlation with the ONI is essentially null (0.019). We performed
236 the same analysis using the Multivariate Enso Index (Wolter and Timlin 2011) and the Southern
237 Oscillation Index (Ropelewski and Jones 1987) to conclude that these results do not depend on the
238 ENSO index used.

c. *Impacts*

The SAM has been shown to be associated with important surface variables such as temperature and precipitation (e.g. Gillett et al. 2006, and see Fogt and Marshall (2020) for a review). Naturally, most studies on the surface impacts of the SAM are based on an index identical or analogous to what we call Full SAM index (Fogt et al. (2012) being the only exception that we are aware of). We regress surface temperature and precipitation onto each of the three SAM indices to see if there are different surface impacts associated with the asymmetric and symmetric SAM circulation.

Figure 10 shows regression coefficients of each index at 700 hPa with surface temperature for each trimester. In Summer positive values of the Full SAM index (panel a.1) are associated with negative temperature anomalies near Antarctica which are surrounded by a ring of positive anomalies. The ring is not zonally symmetric, as there are three clear local maximums around 30°W, 15°E and 50°E and a local minimum (with negative sign) around 120°W. In the tropics, there are negative anomalies in the equatorial Pacific, consistent with the negative correlation between SAM and ENSO. Panels b.1 and c.1 show temperature anomalies associated with positive values of the Asymmetric and Symmetric SAM, respectively. Both the local maximums in the ring and the anomalies in the Pacific regions are present mostly on the Asymmetric SAM regression map, while temperature patterns linked to positive Symmetric SAM show a more zonally consistent ring and less relation to the tropics. Noticeable, temperature anomalies in the Indian ocean, South Africa and Australia are strongly related to positive values of Asymmetric SAM. This signal is not present in the regression pattern with the Full SAM. Spring (row 4) features very similar patterns but of generally smaller in magnitude and statistical significance.

In Autumn and Winter (rows 2 and 3) the positive ring is only present through its local maximums in the regression with the Full SAM. There are also negative anomalies in Southern Australia,

262 and positive anomalies over New Zealand and Southern South America. These patterns are not
263 significant in the sense that there are no areas with p-values below 0.05 when controlling for FDR
264 following Wilks (2016). However, repeating this analysis with 2-meter temperature from ERA5
265 resulted in similar patterns that were statistically significant. Moreover, similar features were
266 observed in station measurements by Jones et al. (2019), although using data from 1957 to 2016.

267 The pattern of negative anomalies in the pole surrounded by positive anomalies roughly seen
268 in all seasons –although with varying intensity and small-scale details– is consistent with the
269 intensification and poleward migration of the westerlies commonly linked to the SAM. It's then not
270 surprising to see it more clearly in association with the Symmetric SAM (at least in Summer and
271 Spring).

272 These results suggests that Asymmetric and Symmetric SAM indices are associated with overall
273 distinct temperature patterns which may not be apparent when using the Full SAM index.

274 Figure 10 column b can be partially compared with Figure 11 from Fogt et al. (2012). Although
275 they used station data from 1958 to 2001, a lot of the characteristics are reproduced here, such as
276 the strong signal in New Zealand and Australia in Summer and Spring.

277 Regression of the SAM indices with seasonal mean precipitation and 700 hPa geopotential
278 height are shown Figures 11 and 12 for Australasia and South America respectively. South Africa
279 is not shown because no significant signal was detected there.

280 In Australia, the annual regression shows that the Full SAM index is positively associated with
281 precipitation in the Southeastern region (Figure 11 panel a.1), which reproduces the results from
282 Gillett et al. (2006). The separation between Asymmetric and Symmetric SAM suggest that
283 this positive anomaly is explained by the Symmetric SAM only in the East coast (panel c.1).
284 Geopotential anomalies associated with this index (black contours) are indicative of easterly flow
285 from the Tasman Sea, which could explain the positive anomalies in precipitation as found by

Hendon et al. (2007). The Asymmetric SAM appears related to increased precipitation in the West coast of Southeastern Australia (panel b.2), which could similarly be explained by the anomalous westerly circulation transporting moist air to the continent from the Indian Ocean.

This Spring signal is broadly consistent with Hendon et al. (2007), but whereas Hendon et al. (2007) also detected a strong signal in Summer, panel a.2 shows no statistically significant association (although the coefficients have the consistent sign).

The seasonal-level regressions show statistically significant anomalies only in Spring, when positive Full SAM is associated with positive precipitation anomalies in Eastern Australia (panel a.5). In this trimester the Symmetric SAM seems to be associated with precipitation in a relatively reduced area of the East Coast (panel c.5) while the positive precipitation anomalies related with positive Asymmetric SAM affect all Eastern Australia (panel b.5).

In Summer, positive Full SAM index is associated with positive precipitation anomalies in Western and Eastern Australia, particularly in the North East (panel a.2). The Eastern part being dominated by the relationship with the Symmetric SAM and the Western, by the Asymmetric SAM. In Autumn, the regression with Full SAM shows positive values in the North, similar to Summer, and a broad area of positive values in the North-East to South-West direction. This structure seems to be associated with the Symmetric SAM, while the Northern positive values are associated with the Asymmetric SAM. In Winter we see the same NE to SW aligned anomaly (although with much reduced amplitude) that is also present only in relation with the Symmetric SAM. None of these regression coefficients are statistically significant at the 95% level

In South America (Figure 12), the annual-level regression shows that the SAM is associated with statistically significant precipitation decrease in Southeastern South America (SESA) and Southern Chile and non-significant increase in South Brazil, near the South Atlantic Convergence Zone (SACZ) (panel a.1). Panels b.1 and c.1 show a remarkably clean separation between the

310 Asymmetric SAM –associated with the Southeastern South American and Southern Brazilian
311 signals– and the Symmetric SAM –associated with the signal in Southern Chile.

312 Except Winter, seasonal-level regressions mirror this same pattern. Even if not statistically
313 significant, they all show negative values in Southeastern South America and Southern Chile
314 along with positive values in Southern Brazil in relation with the Full SAM. The separation of
315 these features between the Asymmetric SAM and Symmetric SAM regression maps is also rather
316 consistent.

317 The anomalous circulation at 700 hPa associated with the Symmetric SAM (panel c.1) indicate
318 anomalous Easterly flow over Southern Chile. This leads to reduced influx of moist air from
319 the Pacific Ocean which, is the main source of precipitable water in that region. On the other
320 hand, the anomalous circulation associated with positive values of Asymmetric SAM (panel b.1)
321 in the Atlantic is anticyclonic in the South and cyclonic in the North. This creates anomalous
322 South-Easterly flow over Southeastern South America, which inhibits the flow of the Low Level
323 Jet to the region (Silvestri and Vera 2009, Zamboni et al. (2010)). This same pattern was found to
324 be associated with increased precipitation in Southern Brazil during South Atlantic Convergence
325 Zone events (Rosso et al. 2018).

326 There is a small area of increased precipitation with SAM near central Argentina which is
327 also present in the station-based analysis by Gillett et al. (2006) and that is explained by the
328 Asymmetric SAM.

329 *d. Conclusions*

330 In this study we tried to systematically characterise the variability of the zonally symmetric and
331 zonally asymmetric structure of the SAM. By projecting monthly geopotential fields at each level

332 with the corresponding asymmetric and symmetric pattern, we created two indices representing
333 the zonally asymmetric and zonally symmetric contributions of the SAM respectively.

334 As expected, the Asymmetric SAM index correlates strongly with the Symmetric SAM index.
335 In the troposphere, this correlation is maximum at zero lag, while in the stratosphere is maximised
336 with the Asymmetric SAM leading the Symmetric SAM by one month. Since most indices of the
337 SAM are calculated using surface or near-surface conditions, this result would suggest that they
338 might not be sensitive to the most dramatic changes in SAM variability.

339 The two-year periodicty we found in the stratospheric Symmetric SAM might point to a link
340 between the SAM and the Quasi Biennial Oscillation. There is evidence of influence between the
341 QBO and the Northern Annular Mode (e.g. Holton and Tan 1980, Watson and Gray (2014), Zhang
342 et al. (2020)), so it's not unlikely that the SAM would be similarly connected. However establishing
343 this link would require further research.

344 As documented by previous studies, such as Fogt and Marshall (2020) (and references therein),
345 we observe a positive trend towards positive SAM in Summer and Autumn. We show that these
346 trends are maximised at the 100 hPa level and are explained by the zonally symmetric component.
347 We also find a statistically significant positive trend in the Symmetric component of the SAM in
348 the stratosphere that is not apparent in the Full SAM index. In contrast to Fogt et al. (2012) we find
349 some evidence of the SAM becoming more zonally asymmetric, as there is a slight positive trend
350 in the variance explained by the as the Asymmetric SAM explains an increasingly proportion of
351 the total variance.

352 In the troposphere, the spatial patterns of geopotential associated with the Symmetric SAM is
353 much closer to being trully annular than the patterns associated with the Full SAM index. The
354 Asymmetric SAM, on the other hand, describes a wave-3 pattern with maximum amplitude in
355 the Pacific region and whose phae is rotated a quarter wavelength from the mean zonal wave 3

described by Raphael (2004)'s index. This pattern extends in the troposphere but its maximum is located at 250 hPa, which also could suggest that surface-based indices are not optimum for capturing this variability.

This wave-3 pattern is similar to the Pacific-South American Pattern, which is a teleconnection pattern linked to ENSO variability. We found that the significant correlation that exists between the Full SAM index and the Oceanic Niño Index is captured entirely by the Asymmetric SAM index. This suggests that ENSO is linked to SAM exclusively through the variability in the latter's Asymmetric component.

Temperature anomalies associated with the Full SAM broadly show a pattern of negative anomalies at polar latitudes surrounded by positive anomalies, but with many deviations from symmetry. The Asymmetric SAM index explains a big portion of these deviations. In particular, the positive phase of the Asymmetric SAM is associated with colder temperatures over Southern Brazil, South Africa and Southern Australia, as well as the negative anomalies in the equatorial Pacific consistent with the ENSO-SAM relationship delineated above. These are particularly clear in the DJF and SON trimesters, which include the months in which the ENSO teleconnection is more active (Cazes-Boezio et al. 2003; Fogt et al. 2011; Cai et al. 2020).

In Australia the Full SAM is associated with positive precipitation anomalies in South East and this is explained by the Symmetric SAM. However, the Asymmetric SAM is associated with a small area of positive precipitation anomalies in the Eastern Coast of West Australia, maybe due to advection of moist air from the Indian Ocean.

In South America, precipitation anomalies associated with the Full SAM are negative both in Southern Chile and Southeastern South America, and positive in Southern Brazil. This features are cleanly separated between the Asymmetric and Symmetric components. The Symmetric SAM explains the negative anomalies in Southern Chile and the Asymmetric SAM, the negative-positive

dipole between Southeastern South America and Southern Brazil. Individual seasons mostly follow this pattern.

Silvestri and Vera (2009) suggests that precipitation impacts linked to the SAM changed rather dramatically before and after 1980. In particular, the negative relationship with precipitation in South America was absent in some areas and switched sign in other in the earlier period. The correlation between ENSO and SAM is similarly non-stationary, also disappearing before 1973.

Seeing as both the ENSO-SAM relationship and most of the precipitation impacts in South America are captured by the Asymmetric SAM, the results presented here are most likely period-dependent. Therefore, it is very likely that if we were to repeat this analysis using pre-satellite data, the resulting Asymmetric SAM would look very different.

Acknowledgments. NOAA Global Surface Temperature (NOAA GlobalTemp) data provided by the NOAA/OAR/ESRL PSL, Boulder, Colorado, USA, from their Web site at <https://psl.noaa.gov/>

References

Baldwin, M. P., 2001: Annular modes in global daily surface pressure. *Geophysical Research Letters*, **28** (21), 4115–4118, doi:10.1029/2001GL013564.

Baldwin, M. P., and T. J. Dunkerton, 2001: Stratospheric Harbingers of Anomalous Weather Regimes. *Science*, **294** (5542), 581–584, doi:10.1126/science.1063315.

Bamston, A. G., M. Chelliah, and S. B. Goldenberg, 1997: Documentation of a highly ENSO-related SST region in the equatorial Pacific: Research note. *Atmosphere-Ocean*, **35** (3), 367–383, doi:10.1080/07055900.1997.9649597.

Benjamini, Y., and Y. Hochberg, 1995: Controlling the False Discovery Rate: A Practical and Powerful Approach to Multiple Testing. *Journal of the Royal Statistical Society: Series B*

(*Methodological*), **57** (1), 289–300, doi:10.1111/j.2517-6161.1995.tb02031.x.

Cai, W., and Coauthors, 2020: Climate impacts of the El Niño–Southern Oscillation on South America. *Nature Reviews Earth & Environment*, **1** (4), 215–231, doi:10.1038/s43017-020-0040-3.

Cazes-Boezio, G., A. W. Robertson, and C. R. Mechoso, 2003: Seasonal Dependence of ENSO Teleconnections over South America and Relationships with Precipitation in Uruguay. *J. Climate*, **16** (8), 1159–1176, doi:10.1175/1520-0442(2003)16<1159:SDOETO>2.0.CO;2.

Chung, C., and S. Nigam, 1999: Weighting of geophysical data in Principal Component Analysis. *Journal of Geophysical Research: Atmospheres*, **104** (D14), 16 925–16 928, doi: 10.1029/1999JD900234.

Fan, K., 2007: Zonal asymmetry of the Antarctic Oscillation. *Geophysical Research Letters*, **34** (2), doi:10.1029/2006GL028045.

Fogt, R. L., D. H. Bromwich, and K. M. Hines, 2011: Understanding the SAM influence on the South Pacific ENSO teleconnection. *Clim Dyn*, **36** (7), 1555–1576, doi: 10.1007/s00382-010-0905-0.

Fogt, R. L., J. M. Jones, and J. Renwick, 2012: Seasonal Zonal Asymmetries in the Southern Annular Mode and Their Impact on Regional Temperature Anomalies. *J. Climate*, **25** (18), 6253–6270, doi:10.1175/JCLI-D-11-00474.1.

Fogt, R. L., and G. J. Marshall, 2020: The Southern Annular Mode: Variability, trends, and climate impacts across the Southern Hemisphere. *WIREs Climate Change*, **11** (4), e652, doi: 10.1002/wcc.652.

- 423 Gillett, N. P., T. D. Kell, and P. D. Jones, 2006: Regional climate impacts of the Southern Annular
424 Mode. *Geophysical Research Letters*, **33** (23), doi:10.1029/2006GL027721.
- 425 Hendon, H. H., D. W. J. Thompson, and M. C. Wheeler, 2007: Australian Rainfall and Surface
426 Temperature Variations Associated with the Southern Hemisphere Annular Mode. *J. Climate*,
427 **20** (11), 2452–2467, doi:10.1175/JCLI4134.1.
- 428 Hersbach, H., and Coauthors, 2020: The ERA5 global reanalysis. *Quarterly Journal of the Royal*
429 *Meteorological Society*, **146** (730), 1999–2049, doi:10.1002/qj.3803.
- 430 Ho, M., A. S. Kiem, and D. C. Verdon-Kidd, 2012: The Southern Annular Mode: A comparison of
431 indices. *Hydrology and Earth System Sciences*, **16** (3), 967–982, doi:10.5194/hess-16-967-2012.
- 432 Holton, J. R., and H.-C. Tan, 1980: The Influence of the Equatorial Quasi-Biennial Os-
433 cillation on the Global Circulation at 50 mb. *J. Atmos. Sci.*, **37** (10), 2200–2208, doi:
434 10.1175/1520-0469(1980)037<2200:TIOTEQ>2.0.CO;2.
- 435 Jones, J. M., R. L. Fogg, M. Widmann, G. J. Marshall, P. D. Jones, and M. Visbeck, 2009: Historical
436 SAM Variability. Part I: Century-Length Seasonal Reconstructions. *J. Climate*, **22** (20), 5319–
437 5345, doi:10.1175/2009JCLI2785.1.
- 438 Jones, M. E., D. H. Bromwich, J. P. Nicolas, J. Carrasco, E. Plavcová, X. Zou, and S.-H. Wang, 2019:
439 Sixty Years of Widespread Warming in the Southern Middle and High Latitudes (1957–2016).
440 *J. Climate*, **32** (20), 6875–6898, doi:10.1175/JCLI-D-18-0565.1.
- 441 Karoly, D. J., 1989: Southern Hemisphere Circulation Features Associated with El Niño-Southern
442 Oscillation Events. *J. Climate*, **2** (11), 1239–1252, doi:10.1175/1520-0442(1989)002<1239:
443 SHCFAW>2.0.CO;2.

444 Katz, R. W., and B. G. Brown, 1991: The problem of multiplicity in research on teleconnections.
 445 *International Journal of Climatology*, **11** (5), 505–513, doi:10.1002/joc.3370110504.

446 Kidson, J. W., 1988: Interannual Variations in the Southern Hemisphere Circulation. *J. Climate*,
 447 **1** (12), 1177–1198, doi:10.1175/1520-0442(1988)001<1177:IVITSH>2.0.CO;2.

448 Mo, K. C., and M. Ghil, 1987: Statistics and Dynamics of Persistent Anomalies. *J. Atmos. Sci.*,
 449 **44** (5), 877–902, doi:10.1175/1520-0469(1987)044<0877:SADOPA>2.0.CO;2.

450 Raphael, M. N., 2004: A zonal wave 3 index for the Southern Hemisphere. *Geophysical Research*
 451 *Letters*, **31** (23), doi:10.1029/2004GL020365.

452 Rogers, J. C., and H. van Loon, 1982: Spatial Variability of Sea Level Pressure and 500 mb
 453 Height Anomalies over the Southern Hemisphere. *Mon. Wea. Rev.*, **110** (10), 1375–1392, doi:
 454 10.1175/1520-0493(1982)110<1375:SVOSLP>2.0.CO;2.

455 Ropelewski, C. F., and P. D. Jones, 1987: An Extension of the Tahiti–Darwin Southern Oscil-
 456 lation Index. *Mon. Wea. Rev.*, **115** (9), 2161–2165, doi:10.1175/1520-0493(1987)115<2161:
 457 AEOTTS>2.0.CO;2.

458 Rosso, F. V., N. T. Boiaski, S. E. T. Ferraz, and T. C. Robles, 2018: Influence of the Antarctic
 459 Oscillation on the South Atlantic Convergence Zone. *Atmosphere*, **9** (11), 431, doi:10.3390/
 460 atmos9110431.

461 Schneider, U., A. Becker, P. Finger, A. Meyer-Christoffer, B. Rudolf, and M. Ziese, 2015: GPCC
 462 Full Data Reanalysis Version 7.0 at 0.5°: Monthly Land-Surface Precipitation from Rain-Gauges
 463 built on GTS-based and Historic Data: Gridded Monthly Totals. Global Precipitation Clima-
 464 tology Centre (GPCC) at Deutscher Wetterdienst, 20 - 270 MB per decadal gzip compressed
 465 NetCDF archive pp., doi:10.5676/DWD_GPCC/FD_M_V7_050.

- 466 Silvestri, G., and C. Vera, 2009: Nonstationary Impacts of the Southern Annular Mode on Southern
467 Hemisphere Climate. *J. Climate*, **22** (22), 6142–6148, doi:10.1175/2009JCLI3036.1.
- 468 Smith, T. M., R. W. Reynolds, T. C. Peterson, and J. Lawrimore, 2008: Improvements to NOAA’s
469 Historical Merged Land–Ocean Surface Temperature Analysis (1880–2006). *J. Climate*, **21** (10),
470 2283–2296, doi:10.1175/2007JCLI2100.1.
- 471 Vose, R. S., and Coauthors, 2012: NOAA’s Merged Land–Ocean Surface Temperature Analysis.
472 *Bull. Amer. Meteor. Soc.*, **93** (11), 1677–1685, doi:10.1175/BAMS-D-11-00241.1.
- 473 Walker, S. G. T., 1914: *Correlation in Seasonal Variations of Weather, III: On the Criterion for*
474 *the Reality of Relationships Or Periodicities*. Meteorological Office.
- 475 Watson, P. A. G., and L. J. Gray, 2014: How Does the Quasi-Biennial Oscillation Affect the
476 Stratospheric Polar Vortex? *J. Atmos. Sci.*, **71** (1), 391–409, doi:10.1175/JAS-D-13-096.1.
- 477 Wilks, D. S., 2016: “The Stippling Shows Statistically Significant Grid Points”: How Research
478 Results are Routinely Overstated and Overinterpreted, and What to Do about It. *Bull. Amer.*
479 *Meteor. Soc.*, **97** (12), 2263–2273, doi:10.1175/BAMS-D-15-00267.1.
- 480 Wolter, K., and M. S. Timlin, 2011: El Niño/Southern Oscillation behaviour since 1871 as diag-
481 nosed in an extended multivariate ENSO index (MEI.ext). *International Journal of Climatology*,
482 **31** (7), 1074–1087, doi:10.1002/joc.2336.
- 483 Zamboni, L., C. R. Mechoso, and F. Kucharski, 2010: Relationships between Upper-Level Circu-
484 lation over South America and Rainfall over Southeastern South America: A Physical Base for
485 Seasonal Predictions. *J. Climate*, **23** (12), 3300–3315, doi:10.1175/2009JCLI3129.1.

486 Zhang, R., W. Tian, and T. Wang, 2020: Role of the quasi-biennial oscillation in the downward
487 extension of stratospheric northern annular mode anomalies. *Clim Dyn*, **55** (3), 595–612, doi:
488 10.1007/s00382-020-05285-4.

APPENDIX

Extra figures

491	LIST OF FIGURES	
492	Fig. 1. Spatial patterns of the first EOF of 700 hPa geopotential height	28
493	Fig. 2. Time series for the Asymmetric SAM and Symmetric SAM indices at (a) 50 hPa and (b) 700	
494	hPa	29
495	Fig. 3. Correlation between the Symmetric SAM and Asymmetric SAM index at each level for lag	
496	zero and lag -1 (Symmetric leads Asymmetric)	30
497	Fig. 4. Cross correlation between levels of the (a) Full SAM, (b) Asymmetric SAM, and (c) Sym-	
498	metric SAM	31
499	Fig. 5. Decadal trends at each level for annual (row 1) and seasonal values (rows 2 to 5) for the	
500	period 1979-2018 and for the (column a) Full SAM index, (column b) Asymmetric SAM	
501	index, and (column c) Symmetric SAM index	32
502	Fig. 6. Decadal trends of the variance explained by the Asymmetric and Symmetric SAM at each	
503	level for the period 1979-2018	33
504	Fig. 7. Regression patterns of geopotential height (meters) at (row 1) 50 hPa and (row 2) 700 hPa	
505	with the (column a) Full SAM, (column b) Asymmetric SAM, and (column c) Symmetric	
506	SAM	34
507	Fig. 8. Amplitude (meters) of zonal waves of the geopotential height regression patterns in Figure	
508	7 for zonal waves with wave-number 0, 1, 2, and 3, where wave-number 0 represents the	
509	amplitude of the zonal mean. Note the different x axis.	35
510	Fig. 9. Regression between monthly geopotential anomalies (meters) averaged between 65° and	
511	40°S and the Asymmetric SAM index (extracted from multiple regression including the	
512	Symmetric SAM)	36
513	Fig. 10. Regression pattern of season mean surface temperature (Kelvin) with Asymmetric SAM and	
514	Symmetric SAM	37
515	Fig. 11. Regression pattern of (row 1) annual and (rows 2 to 5) season mean precipitation anomalies	
516	(mm per day, shading) and 700 hPa geopotential height (thin lines, positive values as solid	
517	lines and negative values as dashed lines) with (column a) Full SAM, (column b) Asymmetric	
518	SAM and (column c) Symmetric SAM	38
519	Fig. 12. Same as Figure 11 but for South America.	39
520	Fig. A1. Lag-correlation between Asymmetric SAM and Symmetric SAM index at each level. Neg-	
521	ative lags imply Symmetric SAM leading Asymmetric SAM and vice versa.	40
522	Fig. A3. Fourier spectrum of each timeseries computed as Fourier transform smoothed with modified	
523	Daniell smoothers with widths 3 and 5. The shading indicates the 95% confidence area derived	
524	by fitting an autoregressive model and computing the spectrum for 5000 simulated samples	
525	from the fitted autoregressive model (95% of the simulated samples had an amplitude equal	
526	or lower). The light line indicates the theoretical expected amplitude from the autoregressive	
527	model.	41

528	Fig. 13.	700 hPa Geopotetnial height zonal anomalies (meters) of composites of positive and negative	
529		SAM months selected using ± 1 standard deviation as threshhld	42
530	Fig. 14.	Regression of 700 hPa geopotential height zonal anomalies (meters) onto the standarised	
531		timeseries of the leading EOF computed for each season independently	43
532	Fig. 15.	Regression of 700 hPa geopotential height zonal anomalies (meters) onto the standarised	
533		timeseries of the leading EOF computed for the periods 1979 to 1998 and 1999 to 2018	44

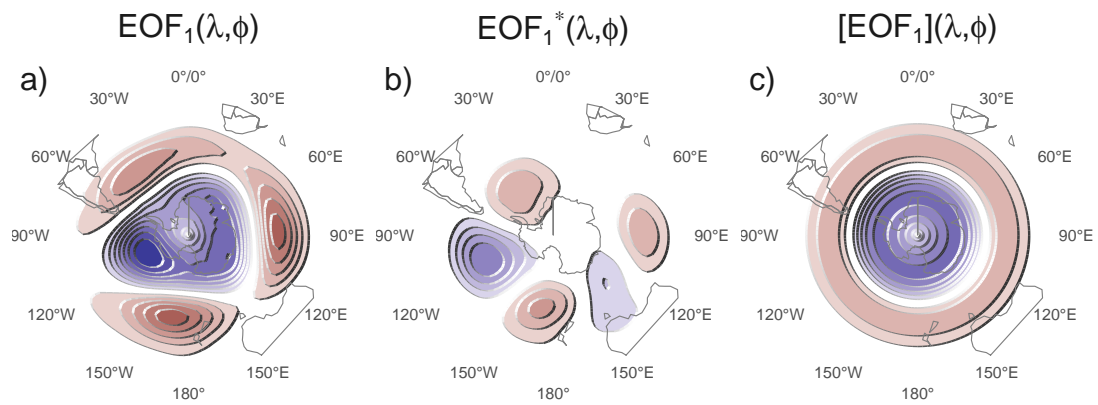


FIG. 1: Spatial patterns of the first EOF of 700 hPa geopotential height. (a) Full field, (b) zonally asymmetric component and (c) zonally symmetric component. Arbitrary units.

fig:method

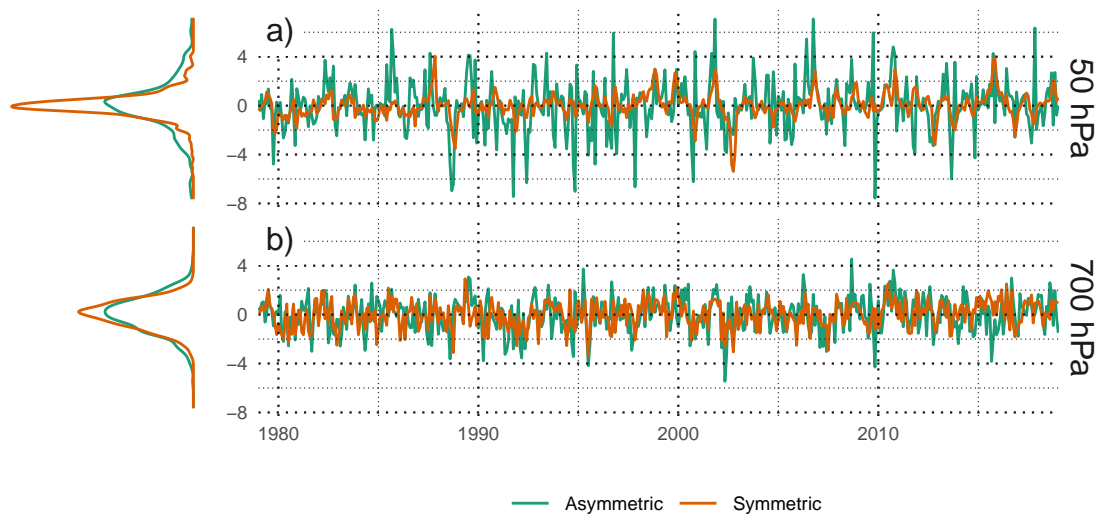


FIG. 2: Time series for the Asymmetric SAM and Symmetric SAM indices at (a) 50 hPa and (b) 700 hPa. To the left, probability density estimate of each index. Series are standardised by the standard deviation of the Full SAM at each level.

fig:asysam-timeseries

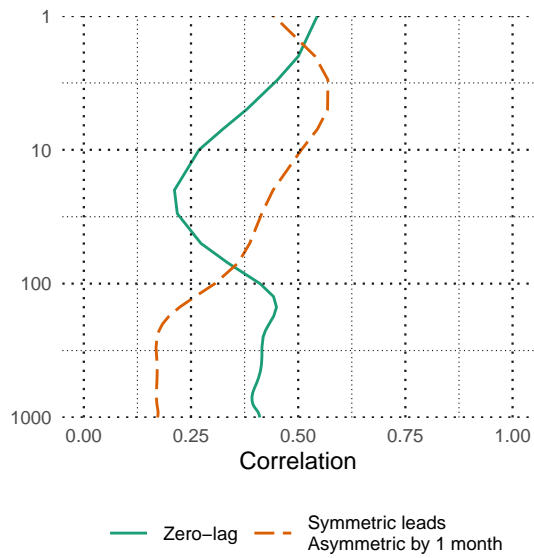


FIG. 3: Correlation between the Symmetric SAM and Asymmetric SAM index at each level for lag zero and lag -1 (Symmetric leads Asymmetric).

fig:cor-lev

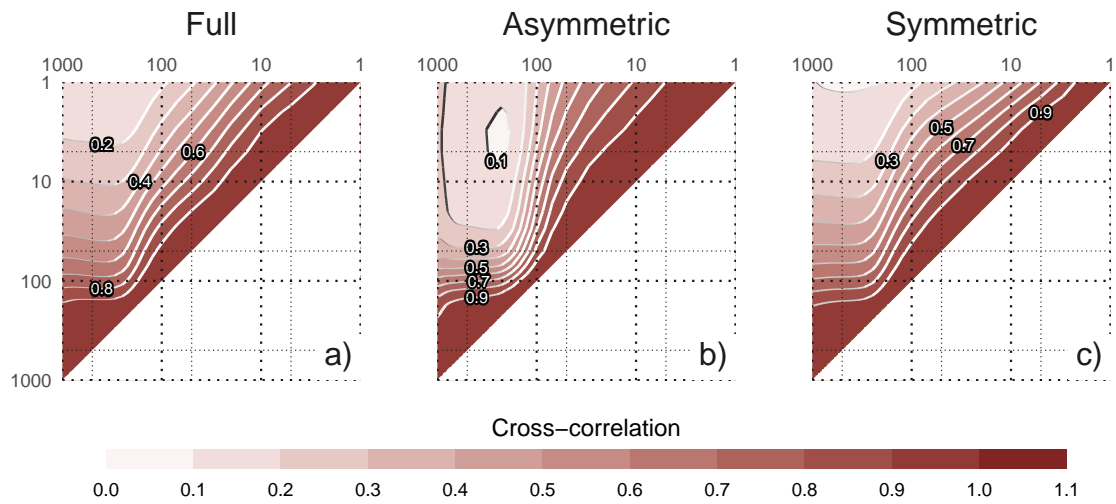


FIG. 4: Cross correlation between levels of the (a) Full SAM, (b) Asymmetric SAM, and (c) Symmetric SAM.

fig:cross-correlation

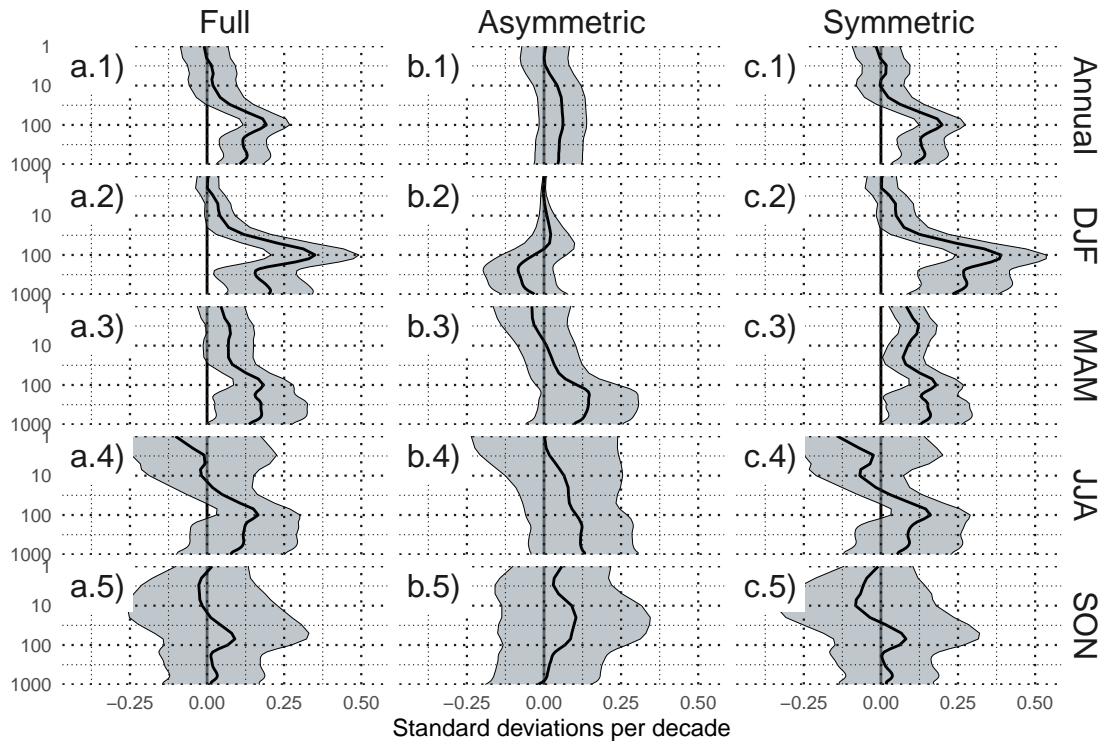


FIG. 5: Decadal trends at each level for annual (row 1) and seasonal values (rows 2 to 5) for the period 1979-2018 and for the (column a) Full SAM index, (column b) Asymmetric SAM index, and (column c) Symmetric SAM index. Shading indicates the 95% confidence interval.

fig:trends

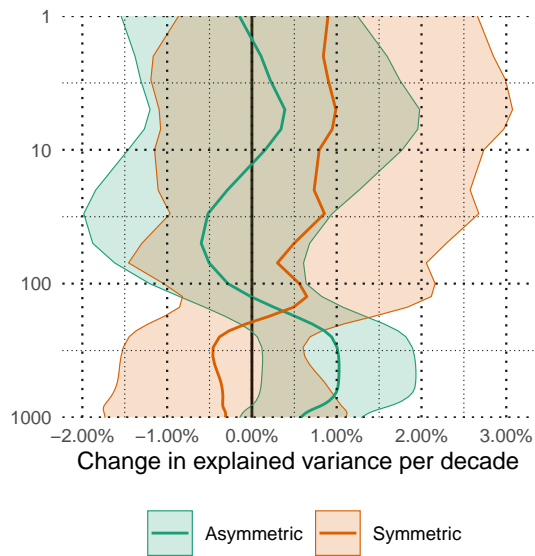


FIG. 6: Decadal trends of the variance explained by the Asymmetric and Symmetric SAM at each level for the period 1979-2018. Shading indicates the 95% confidence interval.

fig:r-squared-trend

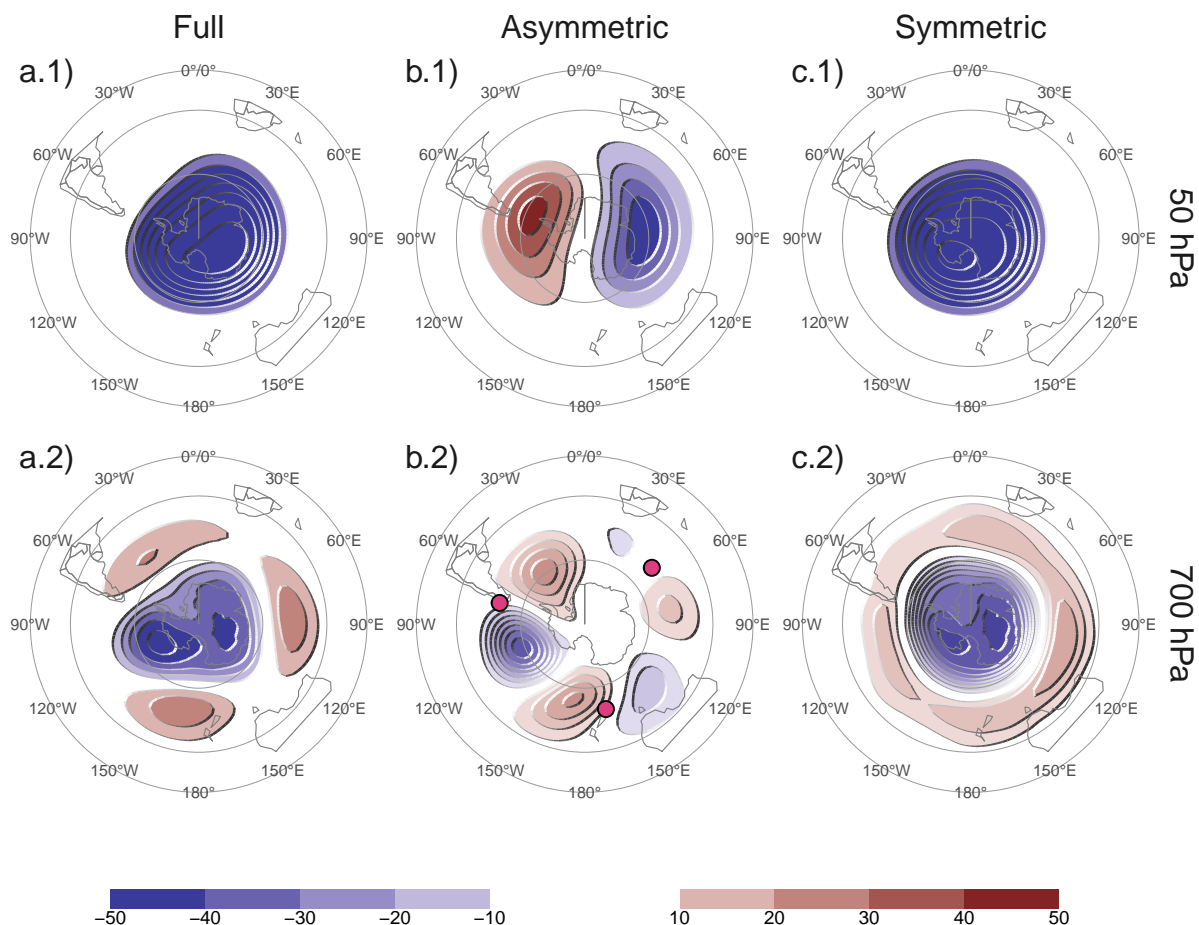


FIG. 7: Regression patterns of geopotential height (meters) at (row 1) 50 hPa and (row 2) 700 hPa with the (column a) Full SAM, (column b) Asymmetric SAM, and (column c) Symmetric SAM. The regression patterns for Asymmetric and Symmetric SAM are the result of one multiple regression using both indices, not of two simple regressions involving each index by itself. Points marked on panel b.2 are the location of the reference points used by Raphael (2004) for their Zonal Wave 3 index.

fig:2d-regr

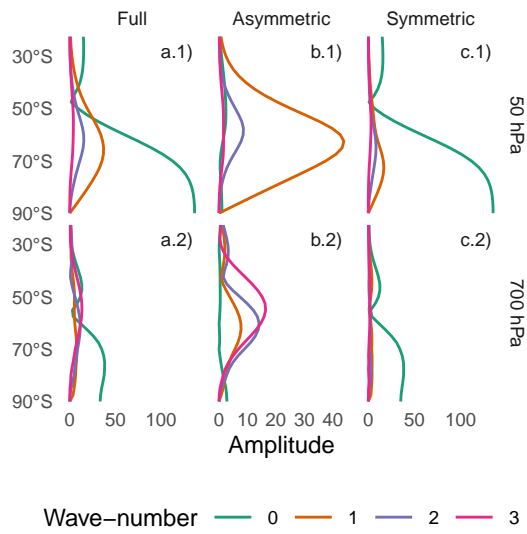


FIG. 8: Amplitude (meters) of zonal waves of the geopotential height regression patterns in Figure 7 for zonal waves with wave-number 0, 1, 2, and 3, where wave-number 0 represents the amplitude of the zonal mean. Note the different x axis.

fig:wave-amplitude

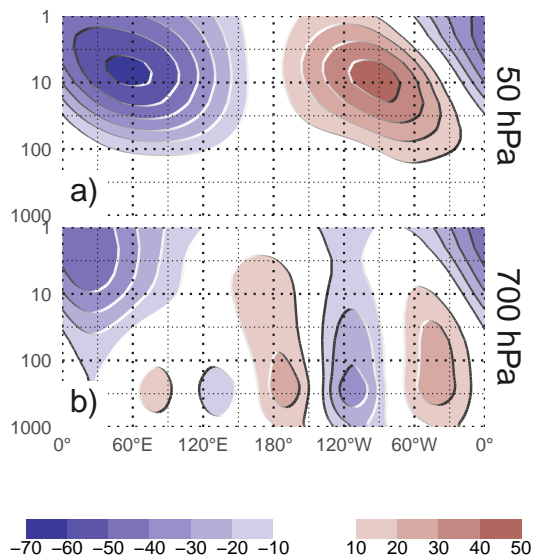


FIG. 9: Regression between monthly geopotential anomalies (meters) averaged between 65° and 40°S and the Asymmetric SAM index (extracted from multiple regression including the Symmetric SAM). (a) With the Asymmetric SAM in 50 hPa and (b) in 700 hPa.

fig:vertical-regression

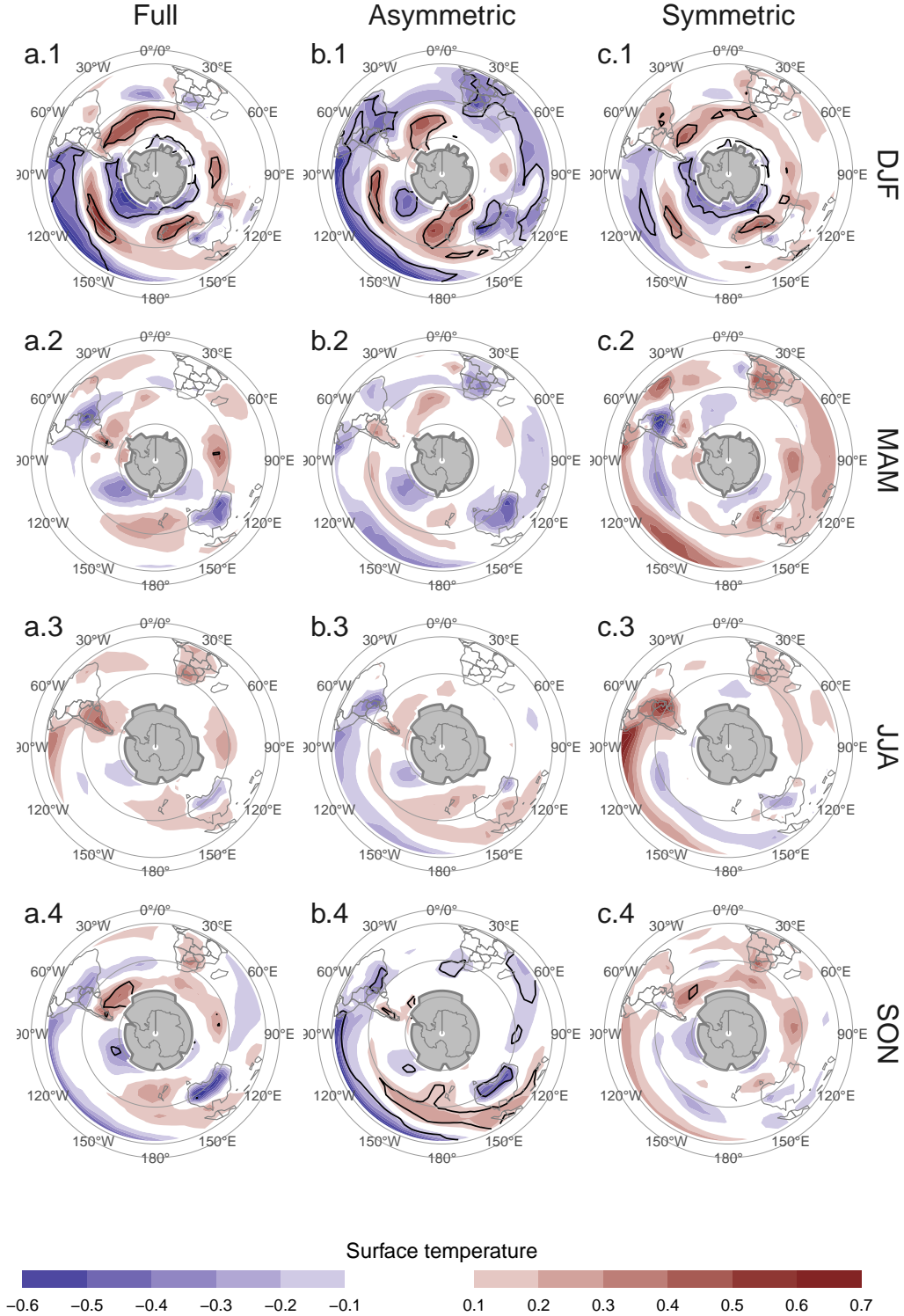


FIG. 10: Regression pattern of season mean surface temperature (Kelvin) with Asymmetric SAM and Symmetric SAM. Black contours indicate areas with p-value smaller than 0.05 controlling for False Detection Rate. Gray areas in Antarctica are areas with have more than 15% of missing data.
fig:regr-air-season

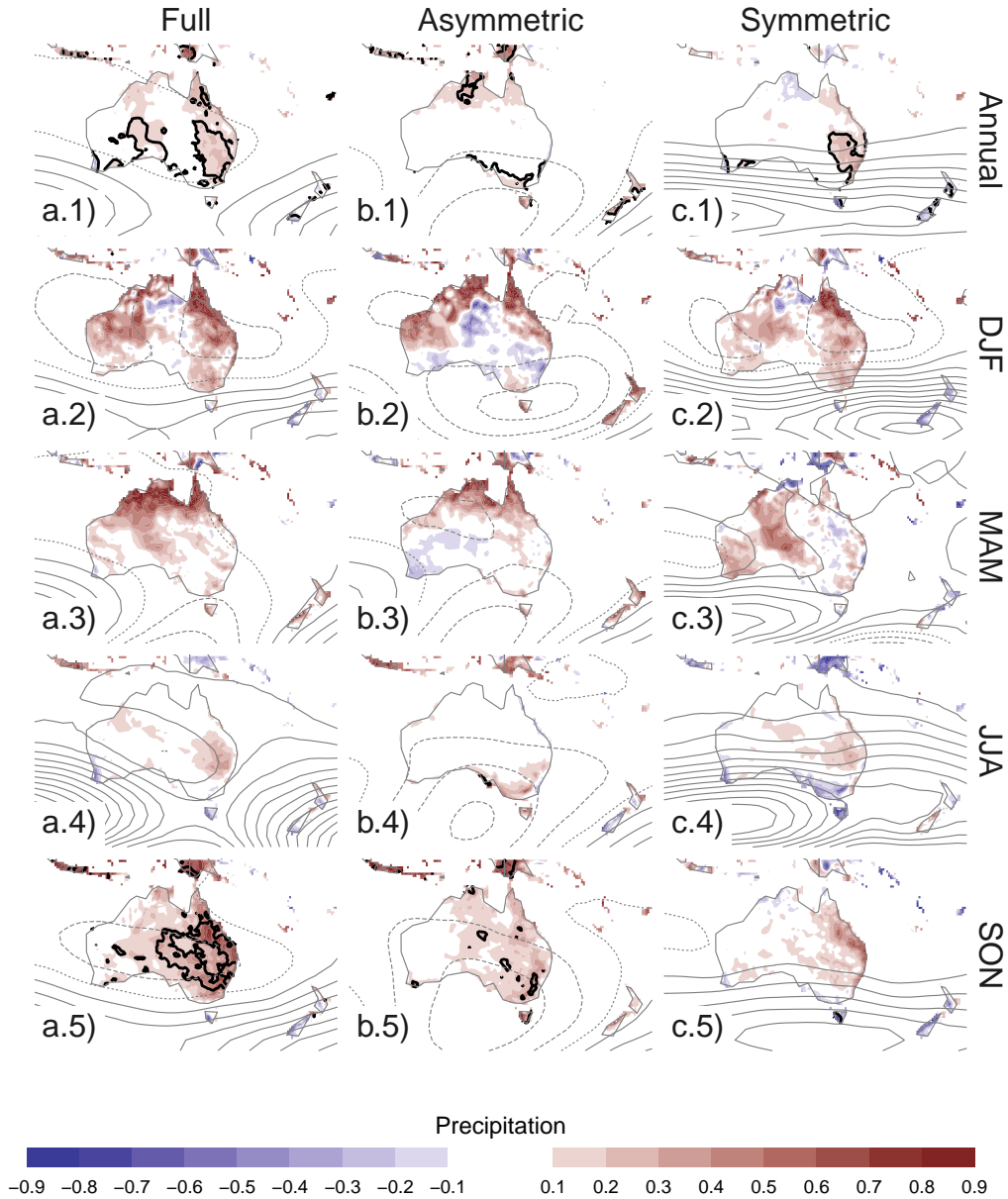


FIG. 11: Regression pattern of (row 1) annual and (rows 2 to 5) season mean precipitation anomalies (mm per day, shading) and 700 hPa geopotential height (thin lines, positive values as solid lines and negative values as dashed lines) with (column a) Full SAM, (column b) Asymmetric SAM and (column c) Symmetric SAM. thin lines are the Black contours indicate areas with p-value smaller than 0.05 controlling for False Detection Rate.

fig:pp-regr-oceania

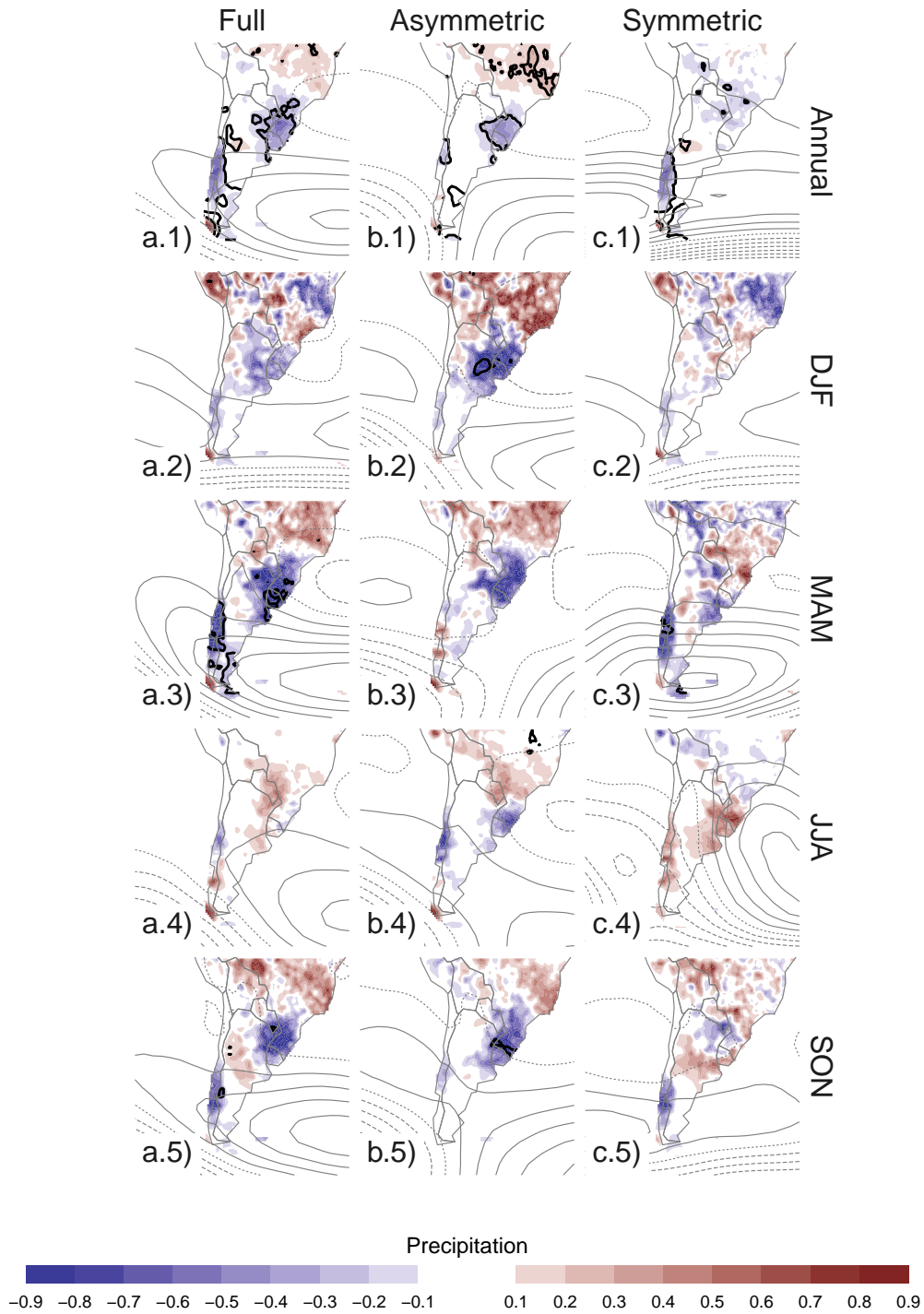


FIG. 12: Same as Figure 11 but for South America.

fig:pp-regr-america

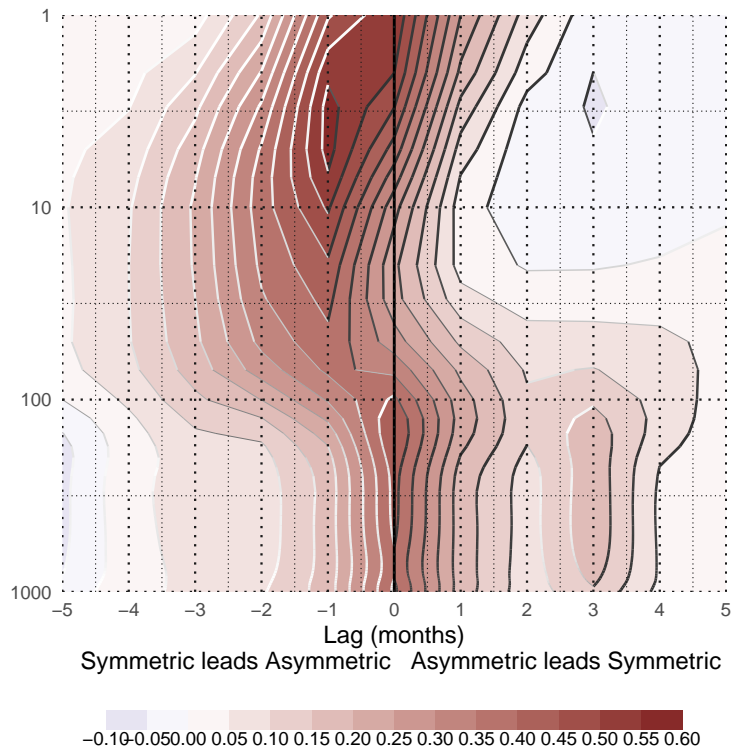


Fig. A1: Lag-correlation between Asymmetric SAM and Symmetric SAM index at each level. Negative lags imply Symmetric SAM leading Asymmetric SAM and vice versa.

fig:A1

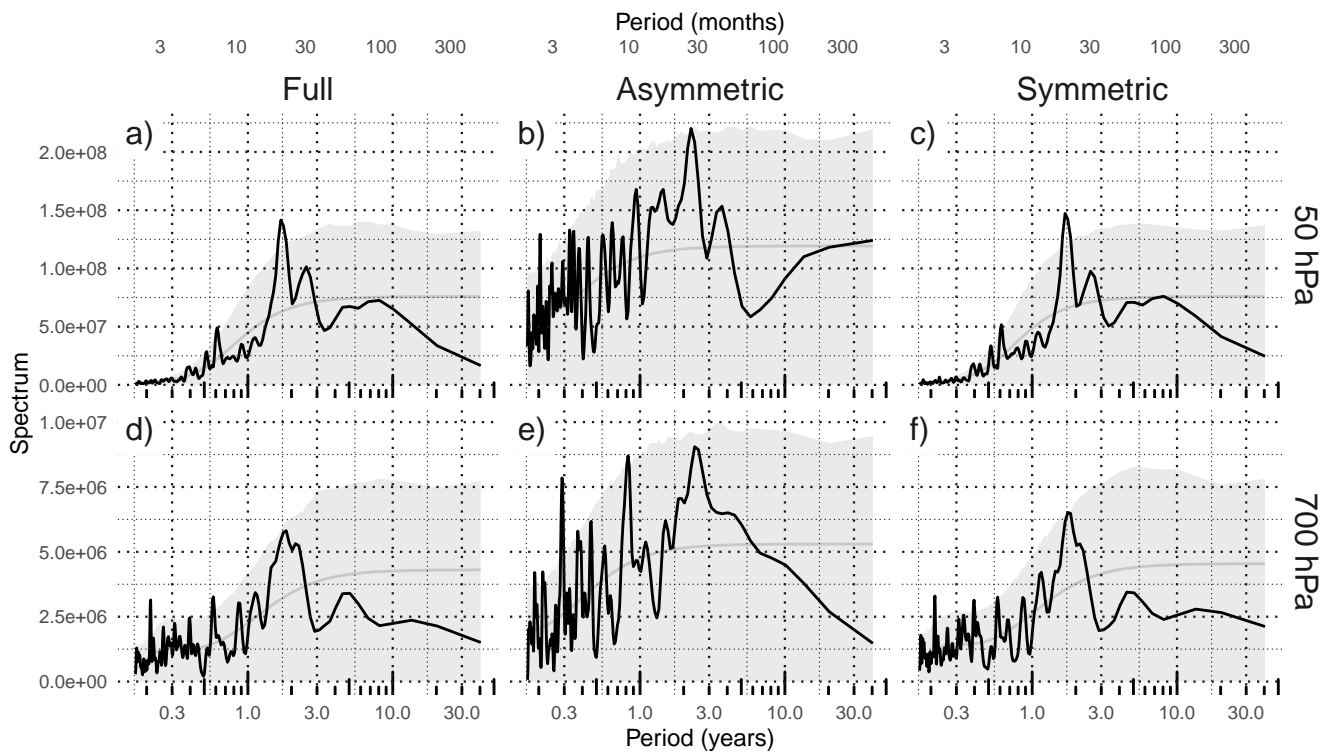


Fig. A3: Fourier spectrum of each timeseries computed as Fourier transform smoothed with modified Daniell smoothers with withs 3 and 5. The shading indicates de 95% confidence area derived by fitting an autorregressive model and computing the spectrum for 5000 simulated samples from the fitted autorregressive model (95% of the simulated sampels had an amplitude equal or lower). The light line indicates the theoretical expected amplitude from the autorregressive model.

fig:A3

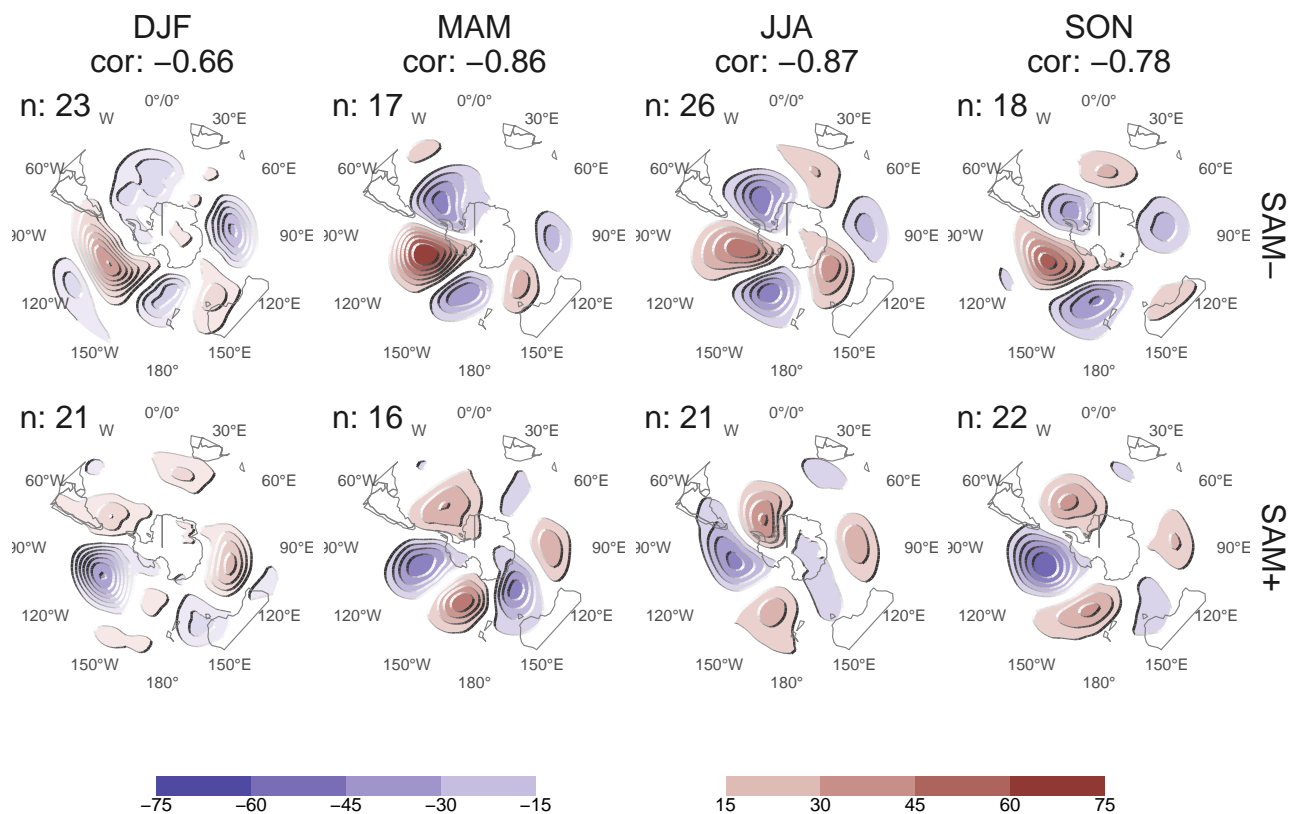


FIG. 13: 700 hPa Geopotential height zonal anomalies (meters) of composites of positive and negative SAM months selected using ± 1 standard deviation as threshold. Numbers in the column headers are pattern correlation between SAM+ and SAM- composites and number of monthly fields used to construct the composites.

fig:A9

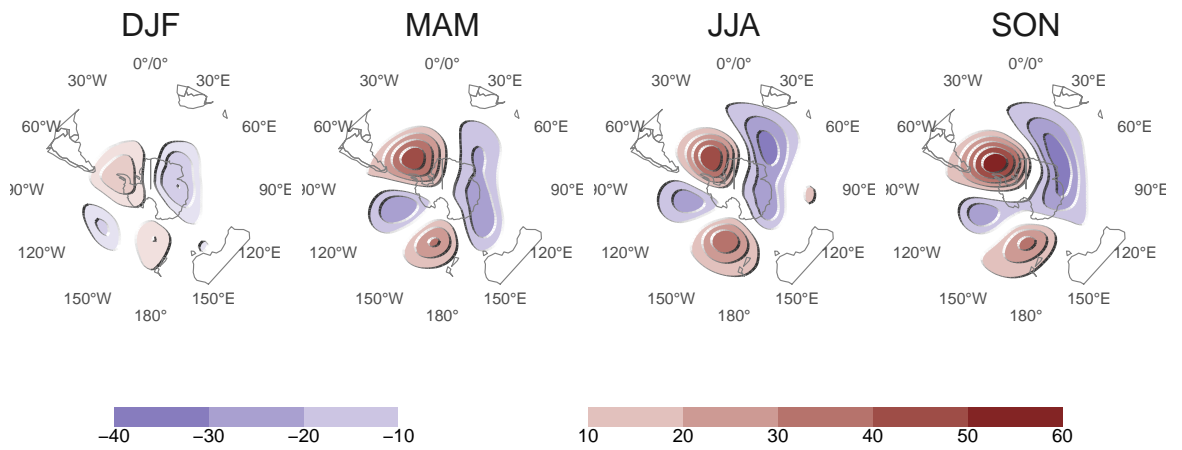


FIG. 14: Regression of 700 hPa geopotential height zonal anomalies (meters) onto the standardised timeseries of the leading EOF computed for each season independently.

fig:A10

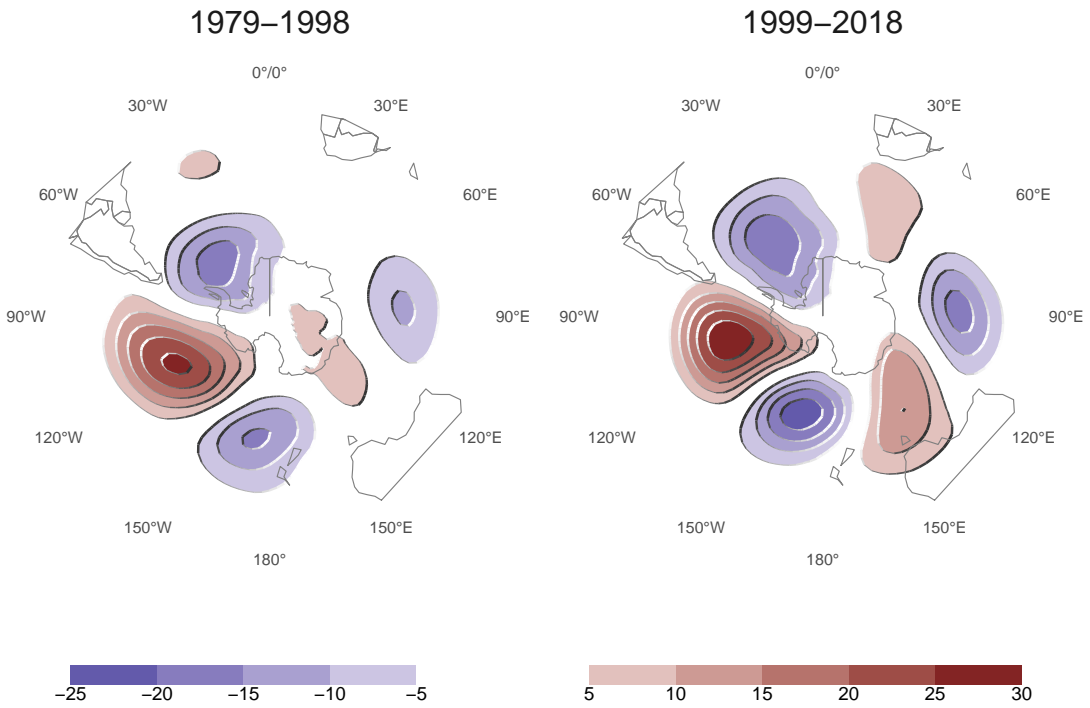


FIG. 15: Regression of 700 hPa geopotential height zonal anomalies (meters) onto the standardised timeseries of the leading EOF computed for the periods 1979 to 1998 and 1999 to 2018. Pattern correlation between both fields is 0.76.

fig:A11